Proceedings of the 4th Jagiellonian Symposium on Advances in Particle Physics and Medicine

Optimization Study of a Muon Tomography System for Imaging of Nuclear Waste Containers

A. Georgadze[a,b,*]

[a] *Institute for Nuclear Research, prospekt Nauky b.47, 03680, Kyiv, Ukraine*
[b] *Institute of Physics, University of Tartu, W. Ostwaldi 1, 50411, Tartu, Estonia*

Doi: 10.12693/APhysPolA.142.391 *e-mail: anzori.heorhadze@ut.ee

For the non-destructive characterization of nuclear waste, muon scattering tomography techniques can be used to image the contents of a concrete-filled steel drum to verify the presence of nuclear materials. The purpose of this study was to compare two possible detector schemes in terms of their performance in localizing nuclear materials. One of the detector schemes consists of two horizontal muon trackers placed above and below the nuclear waste container. Another detector scheme consists of a horizontal upper and a lower tracker and two vertical side trackers. It is expected that side trackers may improve the accuracy of the vertical coordinate determination. For quantitative analysis of detector performance, we have used ROOT CERN tools to perform automated analysis of muon scattering tomography data for detection of dense objects of high-Z materials inside concrete-filled waste drums. GEANT4 toolkit combined with cosmic-ray shower generator was applied to simulate the transport and interactions of muons. Analyzing the simulated data, it was found that due to the loss of energy by muons during ionization processes in the concrete matrix, their spectrum becomes softer, the probability of multiple Coulomb scattering increases, and, accordingly, the muon scattering angles increase. This effect resulted in a point-of-closest-approach signal from the 5 cm tungsten cube placed at the bottom of a nuclear waste container stronger than the signal from the cube at the top. The coordinates (x, y, z) of lead and tungsten cubes were successfully localized in a one-hour measurement time with an accuracy of several millimeters for both detector geometries, indicating that both schemes are compatible.

topics: muon tomography, radioactive waste, particle tracking, GEANT4 toolkit

1. Introduction

Muon tomography (MT) is a rapidly developing new field of science that finds more and more industrial applications, in particular for non-destructively assaying nuclear waste packages [1–5]. It is important to determine the contents of sealed nuclear waste packages before disposal. Therefore there is currently a growing need for novel techniques that could be used to characterize conditioned nuclear waste for the presence of nuclear materials to optimize disposal options.

Muon tomography is a technique that uses cosmic ray muons to scan complex objects. Since muons are highly penetrating and naturally abundant, they offer a unique solution for scanning large dense objects. The most important feature of MT it is uses natural cosmic rays which are harmless, avoiding utilizing hazardous high-energy gamma rays, X-rays, or neutrons, which are used by other scanning techniques. Therefore, MT does not require any artificial radiation source.

Muons are the secondary particles that come from the extensive atmosphere shower of high-energy cosmic rays from space, mainly protons with a flux of about $\approx 10000/\mathrm{m}^2/\mathrm{min}$. The distribution of zenith angle θ is known to follow a cosine-squared law, such that $I(\theta) = I_0 \cos^2(\theta)$. Muons undergo multiple Coulomb scattering in matter, where scattering angle distribution is approximately Gaussian [6, 7]

$$\frac{\mathrm{d}N}{\mathrm{d}\theta} = \frac{1}{\sqrt{2\pi}\theta_0} \exp\left(-\frac{\theta^2}{2\theta_0^2}\right), \tag{1}$$

and the width of the distribution depends on material and muon properties as

$$\theta_0 = \frac{13.6\,\mathrm{MeV}}{cp\beta}\sqrt{\frac{L}{X_0}}\left[1 + 0.038\,\ln\left(\frac{L}{X_0}\right)\right], \tag{2}$$

where β is the ratio between the velocity of muon V and the velocity of light c; p is the momentum of the muon; X_0 is the radiation length of the material; L is the length of the material traversed. It should be noted that X_0 is a material property and depends on the density of the material ρ [g/cm^2], the atomic mass A, and the atomic number Z, and it can be expressed as

$$X_0 = \frac{716.4\,\mathrm{g/cm}^2}{\rho}\frac{A}{Z\,(Z+1)\ln\left(\frac{287}{\sqrt{Z}}\right)}. \tag{3}$$

From (2) and (3), one can see that the width of scattering angle distribution inversely depends on the material radiation length, which is dependent

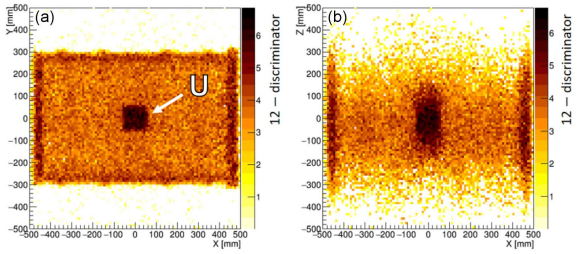

Fig. 1. The reconstructed images of nuclear waste drum (taken from [1]).

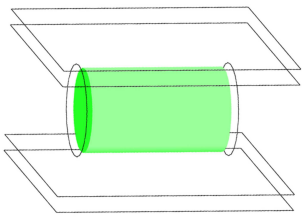

Fig. 2. Illustration of the simulation geometry of two tracking detectors reproduced in GEANT4.

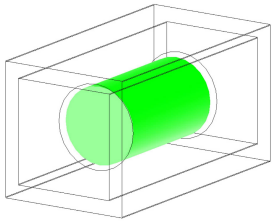

Fig. 3. Illustration of the simulation geometry of four tracking detectors reproduced in GEANT4.

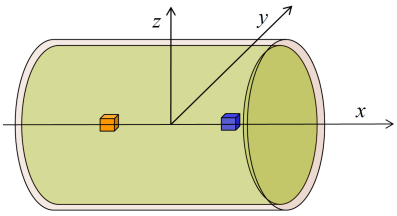

Fig. 4. Illustration of lead and tungsten target locations inside concrete-filled waste drum.

on the atomic number of the material and material density. For materials with higher atomic numbers Z (high-Z), muons will scatter with larger scattering angles. It is therefore possible to characterize the density profile of a large object by measuring muon directions before and after passing through the target object. Besides, scattering angle distribution also inversely depends on muon momentum. For lower muon momentum, larger scattering angles are produced. Muons, like other charged particles, lose energy due to ionization as they traverse dense materials. Being minimum ionization particles, they deposit minimal energy while passing through matter. The scattering angle between the exiting muon track and the incoming muon track can be determined using particle tracking detectors. When developing a tracking detector for muon tomography, it is important to ensure collection of muon tracks from all directions to obtain high quality three-dimensional (3D) image of the target object. Due to the cosine dependence ($\cos^2(\theta)$), the vertical muon flux is several times greater than that of inclined muons with large zenith angles. The lack of the inclined muons, depending on the detector scheme, may result in the smearing effect on the reconstructed image along the z-axis due to the uncertainty caused by the low statistics of near horizontal muon tracks, which give information on the distribution of density and high-Z material in the target object (see Fig. 1).

In this work, Monte Carlo simulations were used to compare the performance of two muon tomography detector schemes that are being developed to reduce the smearing effect shown in Fig. 1 and to improve the accuracy of reconstruction of the z-coordinate of high-Z material objects inside a nuclear waste drum. To quantify the parameters of two detector schemes, we compared the localization accuracy of two 5 cm cubes of lead and tungsten inside the waste drum that each of the detectors can achieve. GEANT4 toolkit combined with cosmic-ray shower generator was applied to simulate the transport and interactions of muons. We have used the ROOT tools to reconstruct the positions of lead and tungsten cubes. To remove noise from a concrete matrix, a clustering algorithm was implemented in the ROOT script.

2. Geometry description and detector layout

The geometry of the muon tomography system was modeled using the GEANT4 simulation package [8]. One of the detector schemes consists of two muon tracking detectors. Each tracking detector consists of two planes of scintillation detectors with a size of 1.5×1.5 m^2. Tracking detectors are placed on the top and bottom sides of the nuclear waste container (1st detector scheme), as shown in Fig. 2. The distance between the top and bottom trackers is 80 cm. Another geometry is a closed type scheme, when muon trackers surround the container from four sides (2nd detector scheme), as shown in Fig. 3. The size of the outer detection plane is 1.5×0.9 m^2, and the inner plane is 1.5×0.7 m^2. The distance between the horizontal and vertical muon trackers 70 cm.

The x- and y-axes are defined as parallel to the ground, while the z-axis is defined as parallel to the normal (see Fig. 4). The distance between the pair of tracking detectors is 10 cm. The top pair of tracking detectors measures the incoming muon track, and the bottom detectors measure the track of outgoing muon.

The simulated concrete-filled drum has a 2.5 cm thick steel wall, an external diameter of 57.4 cm, and a height of 96 cm, and the inner part filled with concrete is 88 cm in height and an internal diameter of 52.4 cm [1]. Inside the waste drum, two target materials were placed, namely a cube of lead with a side length of 5 cm (density 11.35 g/cm^3) at the position (−20 cm, 0, 0) and a cube of tungsten with a side length of 5 cm (density 19.3 g/cm^3) at the position (20 cm, 0, 0) (Fig. 4).

3. Simulation of data samples and muon reconstruction

Simulated data samples are produced using the cosmic ray shower library (CRY) [9], which generates cosmic-ray particle shower distributions with accurate energy and angular distributions of cosmic rays at sea level. The generator is interfaced with a standard GEANT4 package. The cosmic ray muons were generated from a planar surface of a 10 × 10 m^2 area placed above the waste drum. The following formula was used to calculate the scattering angle between two tracks — $\theta_{\text{scatt}} = \arccos(\boldsymbol{v}_{in} \cdot \boldsymbol{v}_{\text{out}})$. The reconstruction of the muon scattering processes was done using the point-of-closest-approach algorithm (PoCA) [10], from which a spatial tree-dimensional distribution of the scattering centers is derived, with a weight proportional to the scattering angle. The PoCA algorithm searches for the geometrical point of closest approach between the incoming $\boldsymbol{v}_{\text{in}}$ and outcoming $\boldsymbol{v}_{out}$ reconstructed track directions with respect to the waste drum. Generated data samples for both detector geometries were produced by propagating 60 million muons at sea level, corresponding to a scanning time of approximately 60 min. For feather analysis only PoCA entries with scattering angles higher than 17 mrad ($\approx 1^\circ$) were considered. This threshold was chosen to allow clear identification of the target objects. We reconstruct the PoCA points with hit positions in the tracking detector smeared simultaneously in x and y directions by Gaussian with a resolution σ of 0.1 mm. Such a resolution corresponds to the detector scheme based on a multiple layer scintillating plastic fiber array as position sensitive detector. The prototype based on such a scheme was constructed [11], and a spatial resolution of 0.15 mm was reached with a double layer array of 1 mm diameter scintillating fibers. Another prototype scintillating-fiber detector system for characterizing encapsulated nuclear waste using cosmic-ray muon tomography has been developed at the University of Glasgow [5].

4. Results and discussion

Upon image reconstruction performed for each data sample, to increase the signal-to-noise ratio and significance of the PoCA signal, the total tree-dimensional PoCA distribution was split into slices

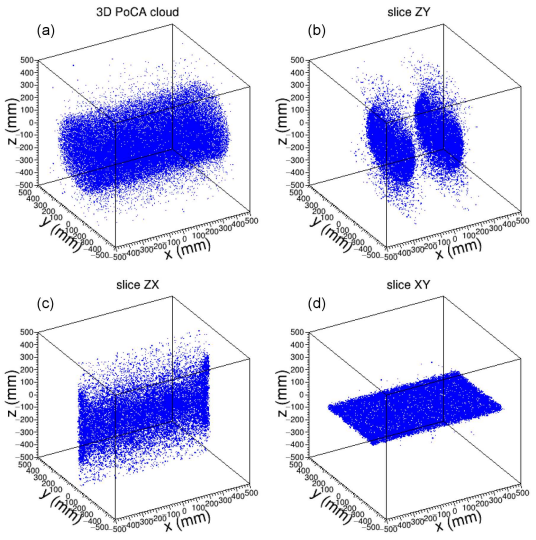

Fig. 5. (a) POCA cloud in 3D view, (b) zy slices at coordinates $x = -20$ cm and $x = 20$ cm, (c) zx slice, (d) xy slice.

along the x-, y-, and z-axes as shown in Fig. 5). The thickness of the slices can be varied to localize high-Z objects of different sizes. To automate the reconstructed PoCA distributions, the three-dimensional (3D) PoCA were projected onto two-dimensional (2D) maps that are easy to analyze using the tools of the ROOT data analysis package [12]. At 2D maps, an increase in the average value of the scattering angle and PoCA density is expected within the small region where a high-Z material is located. Such an increase can be detected using a 2D peak finder implemented in the ROOT tool. Once anomalies in PoCA density are detected, 2D maps can be projected onto one-dimensional (1D) PoCA spectra, which can be processed using the ROOT tool, which allows finding and fitting peaks in the histogram. Found and fitted, the spectrum peaks allow getting information on peak positions and areas. It is also possible to fit 2D maps with a 2D Gaussian function, but we have found that fitting a 1D distribution is faster and easier. As expected, anomalies in PoCA density were found in two vertical zy slices around positions $x = -20$ cm, containing the lead cube, and $x = 20$ cm (Fig. 5b), which has the tungsten cube, and in vertical zx slice (Fig. 5c) around position $y = 0$ cm, and horizontal slice xy (Fig. 5d) around position $z = 0$ cm.

In Figs. 6 and 7, we compare qualitatively 2D projections of reconstructed PoCA images for 1st and 2nd detector schemes. In both figures, bright yellow anomalies correspond to the PoCA signals from lead and tungsten targets. An important feature of these plots is that lead and targets for both detector schemes are well localized in the z direction, and there is no such smearing as in Fig. 1b. This means that both detector geometries supply enough side highly inclined tracks. This means that both

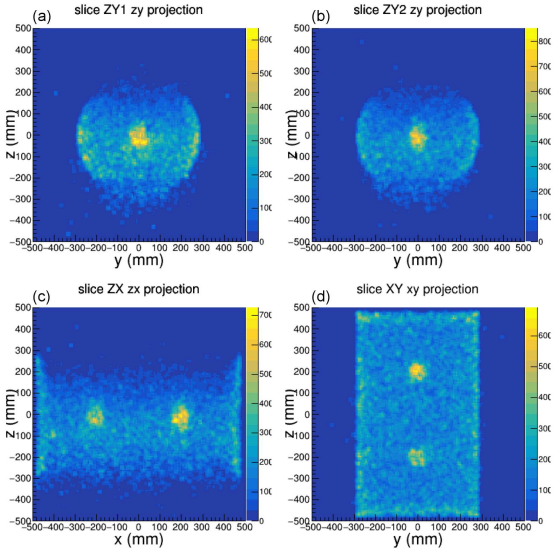

Fig. 6. 2D projections of reconstructed PoCA image for 1st detector scheme.

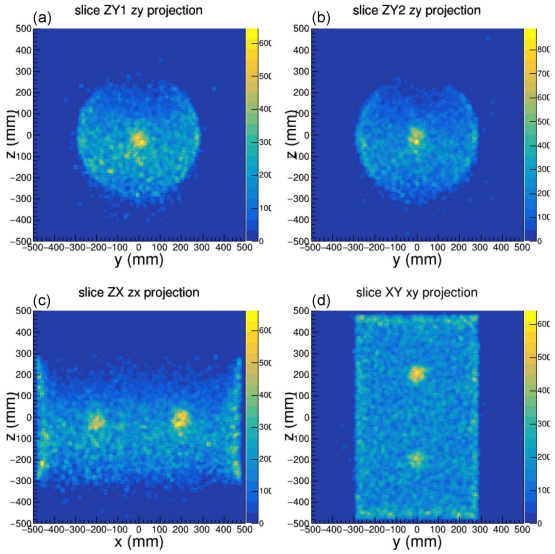

Fig. 7. 2D projections of reconstructed PoCA image for 2nd detector scheme.

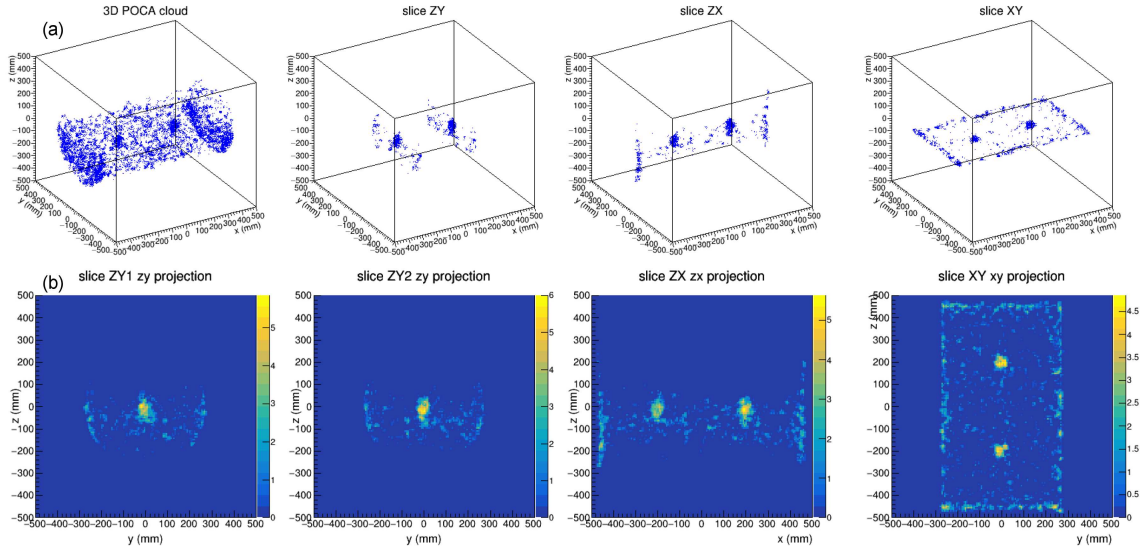

Fig. 8. Reconstructed PoCA images and their 2D and 1D projections after cluster algorithm filtering.

detector geometries provide a sufficient number of highly inclined tracks to perform full 3D target object localization. This is a result of selected detector geometry, which uses in muon tracker thin plastic scintillator planes with a small distance of 10 cm between them. This allows obtaining a wide detector aperture angle $\approx 120°$, providing a good acceptance of the detector to inclined muons. Besides, one can see that qualitatively 2D maps for both detector geometries are very similar, which means that the performance of both detector schemes in the reconstruction of x-, y-, and z-coordinates are compatible.

To remove noise from a concrete matrix, we applied a clustering algorithm. Cluster analysis is a data analysis technique that allows the selection of homogeneous regions in the reconstructed PoCA distribution. The applied algorithm that groups together neighboring voxels according to the principle of signal in a cell, is significant compared to the background noise threshold T. After applying the clustering algorithm, almost all the background from the concrete matrix was removed. Reconstructed images are shown in Fig. 8. However, as is clearly seen in Fig. 8b, some background halo remains and cannot be removed using cluster filtering without affecting the signal.

In the next step, we combined all zy, zx, and xy slices to limit the areas where high-Z targets are located. As a result of the intersection of 3D slices, two cubic regions are cut out from the total 3D PoCA cloud (see Fig. 9).

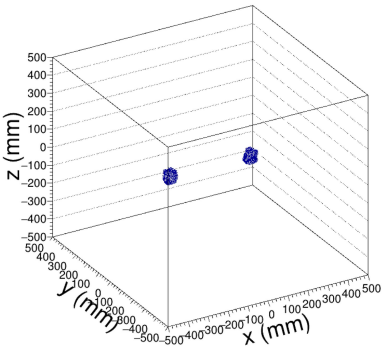

Fig. 9. PoCA image after combining all slices.

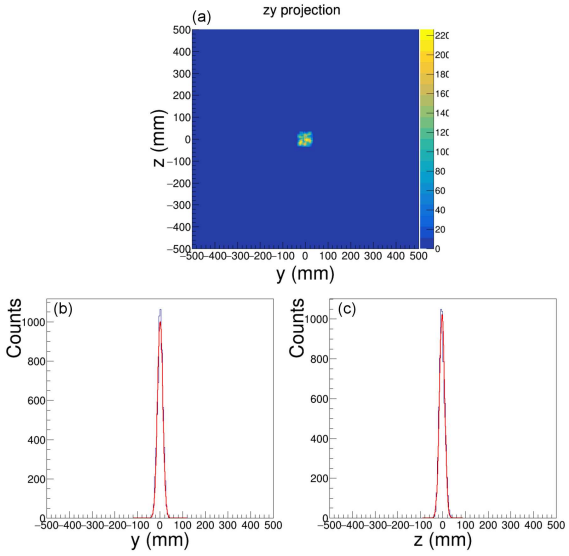

Fig. 10. 2D zy projection of selected PoCA region at position $x = -20$ cm (see text for details).

Figure 10 shows the two-dimensional zy projection of the selected cubic region of the PoCA cloud at position $x = -20$ cm along with its 1D projections. In Fig. 10b, the one-dimensional projection on the y-axis shows a clear distribution in the form of a peak, which is approximated by a Gaussian function. The peak centroid position, μ, corresponds to the lead target y-coordinate with the standard deviation, σ, representing the position uncertainty. The area of the fitted peak distribution corresponds to the PoCA signal with a weight proportional to scattering angle θ and characterizes the density and Z value of the target material. In Fig. 10c, the 1D projection on the z-axis fitted with the Gaussian function is shown. The mean of Gaussian corresponds to the z-coordinate of the lead target.

In Fig. 11, the two-dimensional zy projection of a selected cubic region of the PoCA cloud at the position $x = 20$ cm and its 1D projections are plotted. The mean values of Gaussian fits of 1D projections on the y- and z-axes correspond to the y- and z-coordinates of the tungsten target, respectively.

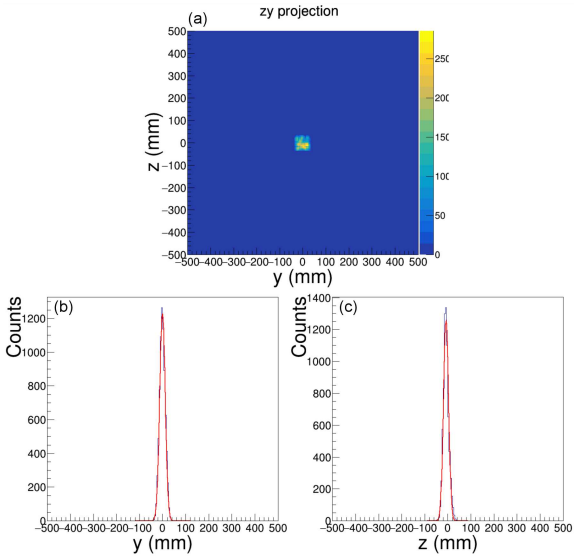

Fig. 11. 2D zy projection of selected PoCA region at position $x = 20$ cm.

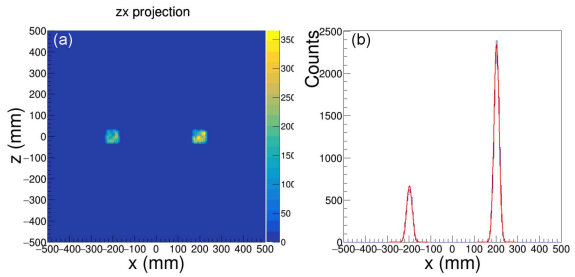

Fig. 12. 2D zx projection of selected PoCA regions.

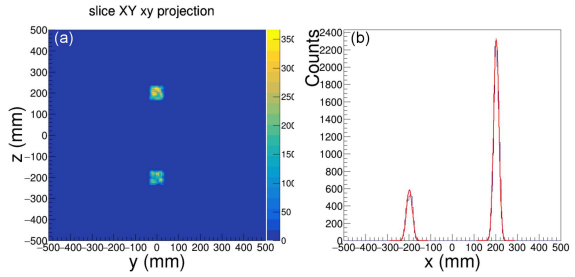

Fig. 13. 2D xy projection of selected PoCA regions.

The area of the fitted peak distribution, corresponding to the PoCA signal weighted with the scattering angle, characterizes the density and the Z value of the target material.

Figure 12 shows the two-dimensional zx projection of a selected cubic region of the PoCA cloud and its 1D projection on the x-axis. Two distributions in the form of a peak are localized around positions $x = -20$ cm and $x = 20$ cm and are well fitted with the Gaussian function. This pro-

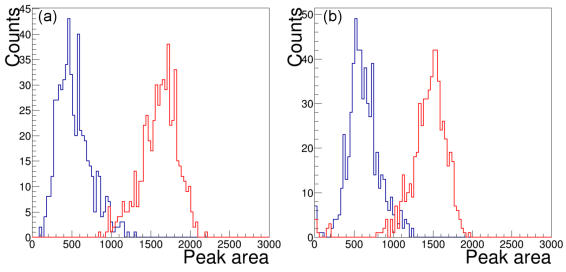

Fig. 14. Distributions of accumulated peak areas for lead (blue line) and tungsten (red line) plotted for 1s detector scheme (a) and 2nd one (b) representing discrimination efficiency.

TABLE I

Reconstructed coordinates of lead and tungsten targets.

	x [mm]	y [mm]	z [mm]
Lead			
1st scheme	-199 ± 5	-0.2 ± 4.2	-9.8 ± 4.1
2nd scheme	-199 ± 3	0.13 ± 2.1	-2.7 ± 2.2
Tungsten			
1st scheme	199 ± 3	0.2 ± 3.6	-10.3 ± 3.8
2nd scheme	200 ± 2	0.1 ± 1.9	-2.9 ± 2.3

jection corresponds to a side view of the cylindrical drum surface. Figure 13 plots the two-dimensional xy projection of selected cubic region and its 1D projection on the x-axis. Two distributions in the form of a peak are localized, as expected, around positions $x = -20$ cm and $x = 20$ cm and well fitted with the Gaussian function. This projection correspond to a the top view of the cylindrical drum surface.

Such a data analysis procedure was performed for all data samples for both detector schemes. By analyzing all the simulated data samples in the following way, the mean values of the Gaussian fits and their area were saved for further analysis. By plotting the accumulated data of Gaussian mean values on a histogram, we obtain the distribution of reconstructed positions of lead and tungsten targets for all data samples. The obtained distributions of centroid positions for each coordinate axis for both detector geometries were fitted with the Gaussian function (Figs. 14 and 15). The peak centroid position, μ, corresponds to the location coordinates of lead and tungsten targets, with the standard deviation, σ, representing the position uncertainty. Reconstructed coordinate values $\mu \pm \sigma$ for both detector geometries are summarized in Table I.

Ability to characterize materials of detected targets was evaluated. As one can see in Figs. 12 and 13, the PoCA signal at location -20 cm corresponding to the lead target is weaker the than signal at position 20 cm, which belongs to tungsten. Accumulated peak areas calculated for all data samples

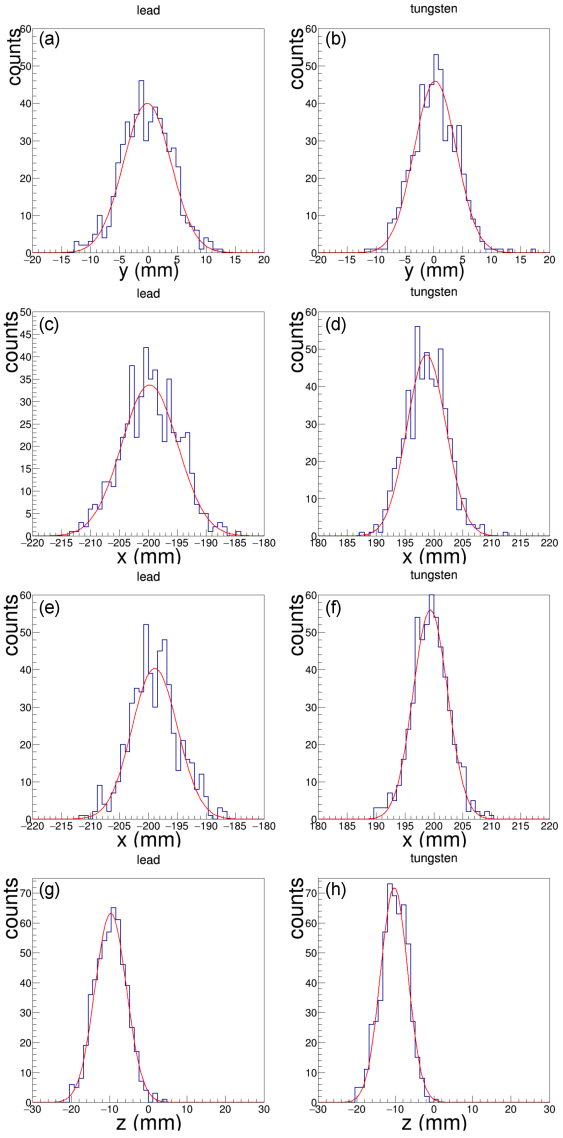

Fig. 15. Gaussian mean values of positions of lead and tungsten targets of all data samples for 1st detector scheme.

are plotted in Fig. 16. For both detector schemes, peak area distributions are almost fully separated, but a longer measurement time is needed for more reliable material discrimination.

As was mentioned before, some background halo remains and cannot be removed using cluster filtering Fig. 8b. In our opinion, this effect can be explained by the increased probability of multiple Coulomb scattering of muons due to the softening of the muon spectrum during the passage of muons through the concrete matrix of the drum. As a result, the number of reconstructed PoCA points and their scattering angles increases to the bottom of the waste drum. As follows from (2), the distribution of scattering angles of muons is inversely proportional to their momentum. For a smaller muon momentum, large scattering angles are created. Muons, like other charged particles, lose en-

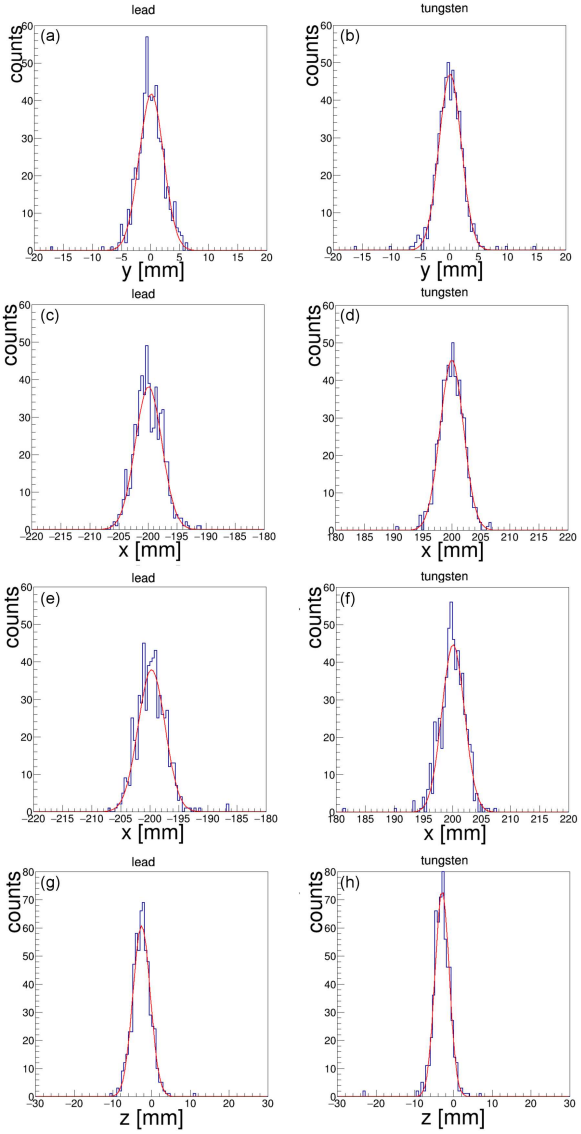

Fig. 16. Gaussian mean values of positions of lead and tungsten targets of all data samples for 2nd detector scheme.

ergy due to ionization as they pass through dense materials. Being particles with minimal ionization, they deposit roughly $\mathrm{d}E/\mathrm{d}x \approx 2$ MeV/g/cm^2 when passing through matter. To test this assumption, we simulated a waste drum filled only with a concrete matrix for 10 h of measurement and selected two 20 cm cube-shaped areas from the 3D PoCA cloud, one near the top of the drum and the other at the bottom (see Fig. 17). The distributions of scattering angles for the upper (blue line) and lower (red line) selected areas are plotted in Fig. 18. The distributions of muon energies for the upper (blue line) and lower (red line) selected areas scaled to the same number of events is plotted in Fig. 19. One can see an excess of low energy muons in the range 0–1 GeV. The presented data confirm the hypothesis of an increase in the angle of scattering to the bottom of the drum.

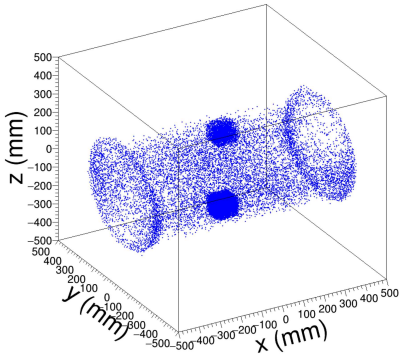

Fig. 17. Illustration of selection of PoCA cube-shaped areas at top and bottom of waste drum.

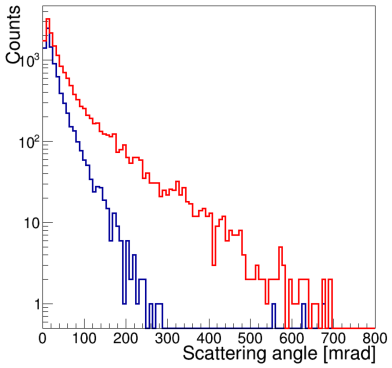

Fig. 18. Scattering angles obtained from simulated data for top (blue line) and bottom (red line) PoCA areas.

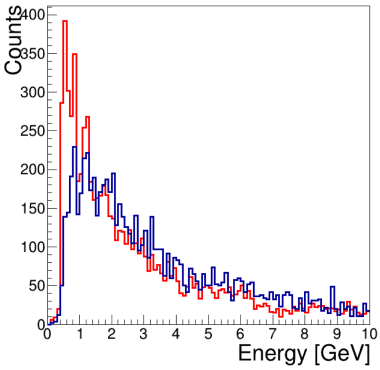

Fig. 19. Muon energies for top (blue line) and bottom (red line) PoCA areas.

To further investigate the impact of this effect on the reconstruction of high-Z objects, we have simulated two 5 cm tungsten cubes, one of which was placed on the top of the nuclear waste drum and the other on the bottom (see Fig. 20a). Figure 20b and c shows a PoCA reconstruction of two tungsten cubes and its projections. As can be clearly seen on the histogram in Fig. 20d, the PoCA signal of the tungsten cube in the upper position inside the drum ($z = 200$ cm) is much weaker than the

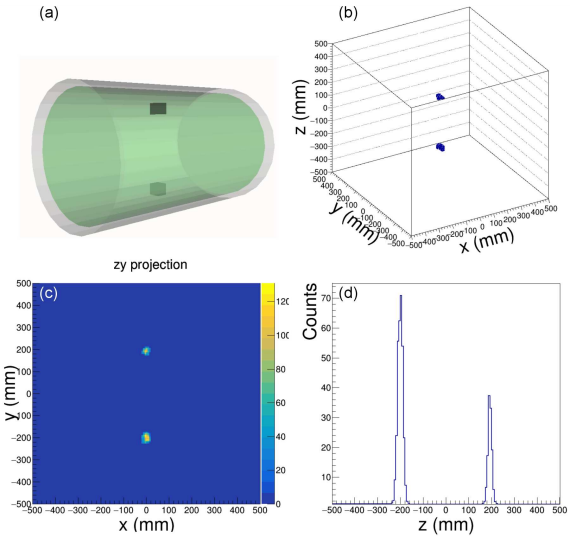

Fig. 20. (a) Illustration of positioning of two tungsten cubes, (b) 3D PoCA reconstruction of two tungsten cubes, (c) 2D projection, (d) 1D projection of PoCA signal are drawn.

signal of the other tungsten cube in the lower position ($z = -200$ cm). This effect requires further detailed study by creating data samples with targets of different sizes and from different materials in different places inside the drum. This effect must be taken into account for the correct classification of high-Z materials depending on their position within the concrete matrix.

5. Conclusions

The results of evaluating the performance of two detector schemes developed for muon tomography of conditioned nuclear waste are presented. To quantitatively study the detector parameters, we apply a simple approach based on PoCA image reconstruction and the ROOT data analysis package to analyze the simulated data. This method allows us to create a container image, remove the background from the concrete matrix, and localize a high-Z object inside the waste drum. One can see from the results shown in Table I that the localized lead and tungsten targets (x, y, z) coordinates are in excellent agreement with the known values with an accuracy better than of 1 cm for both detector geometries, except z-coordinate. We consider that this effect is the result of asymmetry of the muon flux. Muons mostly come from above and rarely in a horizontal direction, but correct localization along the z-axis is possible with an angular coverage of 4π steradians. In addition, it was found that the probability of multiple Coulomb scattering of muons in concrete increases towards the bottom of the drum, so after cluster filtering, there is still a background under the peak distribution, causing a downward shift in the center of gravity of distribution and, accordingly, the mean value of the Gaussian fit.

The results of Monte Carlo simulations and image reconstruction allow us to conclude that the closed-type detector scheme with four trackers does not over-perform the scheme with two muon trackers on top and bottom of the waste drum. We explain this compatibility by the fact that the detector scheme with two trackers provides a wide aperture that allows to reconstruct enough highly inclined muon tracks to allow good accuracy for the reconstruction of the z-coordinate. Therefore we can summarize that both detector schemes have compatible performance for high-Z materials detection and localization.

References

[1] M.J. Weekes, A.F. Alrheli, D. Barker, D. Kikoła, A.K. Kopp, M. Mhaidra, J.P. Stowell, L.F. Thompson, J.J. Velthuis, *J. Instum.* **16**, P05007 (2021).

[2] A. Kopp, A. Alrheli, D. Kikoła, M. Mhaidra, P. Stowell, H. Tietze-Jaensch, M. Weekes, *EPJ Web Conf.* **225**, 06008 (2020).

[3] C. Thomay, J. Velthuis, T. Poffley, P. Baesso, D. Cussans, L. Frazão, *J. Instum.* **11**, P03008 (2016).

[4] L. Frazão, J.J. Velthuis, S. Maddrell-Mander, C.Thomay, *J. Instum.* **14**, P08005 (2019).

[5] A. Clarkson, D.G Ireland, R. Al Jebali et al., in: *2015 4th Int. Conf. on Advancements in Nuclear Instrumentation Measurement Methods and their Applications (ANIMMA), Lisbon 2015*, IEEE, 2016.

[6] S. Eidelman, K.G. Hayes, K.A. Olive et al., Particle Data Group Collaboration, *Phys. Lett. B* **592**, 1 (2004).

[7] G.R. Lynch, O.I. Dahl, *Nucl. Instrum. Methods Phys. Res. B* **58**, 6 (1991).

[8] S. Agostinelli, J. Allison, K. Amako, J. Apostolakis, H. Araujo, P. Arce, D. Zschiesche, *Nucl. Instrum. Methods Phys. Res. A* **506**, 250 (2003).

[9] C. Hagmann, D. Lange, D. Wright, in: *2007 IEEE Nuclear Science Symposium Conference Record, Honolulu (HI) 2007* Vol. 2, IEEE 2008, p. 1143.

[10] D. Sunday, *Practical Geometry Algorithms: With C++ Code*, KDP Print, 2021.

[11] G. Anbarjafari, A. Anier, E. Avots et al., arXiv:2102.12542 (2021).

[12] R. Brun, F. Rademakers, *Nucl. Instrum. Methods Phys. Res. A* **389**, 81 (1997).